PHYSICAL REVIEW D

PARTICLES AND FIELDS

THIRD SERIES, VOLUME 36, NUMBER 3 1 AUGUST 1987

Measurement of antineutron-proton total and annihilation cross sections from 100 to 500 MeV/c

T. Armstrong,[a] C. Chu,[b] J. Clement,[c] C. Elinon,[a] M. Furic,[b] K. Hartman,[a] A. Hicks,[a] E. Hungerford,[b] T. Kishimoto,[b] J. Kruk,[c] R. Lewis,[a] D. Lowenstein,[d] W. Lochstet,[a] B. Mayes,[b] R. Moss,[c] G. S. Mutchler,[c] L. Pinsky,[b] G. A. Smith,[a] L. Tang,[b] W. von Witsch,[c] and Y. Xue[b]

[a]*Laboratory for Elementary Particle Science, Department of Physics, The Pennsylvania State University, University Park, Pennsylvania 16802*

[b]*Department of Physics, University of Houston, Houston, Texas 77004*

[c]*T. W. Bonner Nuclear Laboratory, Rice University, Houston, Texas 77001*

[d]*AGS Department, Brookhaven National Laboratory, Upton, New York 11973*

(Brookhaven–Houston–Pennsylvania State–Rice Collaboration)

(Received 15 January 1987)

Total and annihilation $\bar{n}p$ cross sections from 100 to 500 MeV/c are reported, the first such measurements with good statistics in this momentum range. These cross sections are well represented by $A+B/p$, where p is the incident antineutron momentum, and are in agreement with previous $\bar{n}p$ and $\bar{p}n$ measurements. A comparison of these cross sections with phenomenological potential model calculations is good overall. However, the microscopic quark model gives unsatisfactory predictions. The agreement between previous $\bar{p}p$ annihilation cross sections and $\bar{n}p$ cross sections above 300 MeV/c is excellent. The total $\bar{n}p$ cross section is lower than the total $\bar{p}p$ cross section in this momentum range. Both of these types of behavior are predicted by potential models. The anticipated availability of future $\bar{p}p$ data below 300 MeV/c should indicate whether these trends continue at lower momenta.

I. INTRODUCTION

The measurement of $\bar{N}N$ cross sections in the low-energy regime (defined here as <0.5 GeV/c projectile momentum) has been the source of considerable interest since the discovery of the antiproton over thirty years ago. The motivation from this comes from two distinct, but not unrelated, goals: (i) identification of new narrow states predicted by phenomenological potential models and more recent microscopic quark-gluon bag models and (ii) measurement of other features, such as spin and isospin dependence, of cross sections which would help clarify the underlying physics of the $\bar{N}N$ interactions. Ultimately it is hoped that such data would lead to an understanding of $\bar{N}N$ annihilation in the context of QCD, the present theory of the strong interactions.

Since the $\bar{n}p$ system is pure $I=1$, a measurement of $\bar{n}p$ cross sections should lead to an unambiguous determination of the isospin dependence in the $\bar{N}N$ interaction. To date, only one crude measurement of $\bar{n}p$ annihilation cross sections has been published.[1] In addition, a measurement of $\bar{p}n$ annihilation, which should be identical to $\bar{n}p$ by C invariance, in a deuterium bubble-chamber experiment has been reported.[2] The present experiment studied $\bar{n}p$ total and annihilation cross sections from 100 to 500 MeV/c. The experiment was performed at the Brookhaven National Laboratory Alternating Gradient Synchrotron (AGS). First results from this experiment on the search for narrow states have been published previously,[3] and will not be discussed further in this paper.

The paper is organized as follows: theoretical models are discussed in Secs. II and III; the experimental situation prior to this experiment is reviewed in Sec. IV; apparatus and data-analysis procedures are outlined in Secs. V and VI; and the determination of cross sections with discussion follows in Secs. VII and VIII. Further details may be found in two Ph.D. theses which resulted from this work.[4,5]

II. PHENOMENOLOGICAL POTENTIAL MODELS

In 1949, before the discovery of the antiproton, Fermi and Yang[6] noted that certain repulsive nucleon-nucleon forces could become attractive in the $N\bar{N}$ system. They also predicted that there may exist many bound states due to this effect. These observations set the stage for study-

ing the $N\bar{N}$ system in terms of a potential model framework.

The real (nonannihilation) part of the $N\bar{N}$ potential can be derived from its NN counterpart. In the conventional picture of the NN interaction,[7–9] a potential is generated by the exchange of light, nonstrange scalar (S^*,δ,ϵ), pseudoscalar (π,η,η'), and vector (ρ,ϕ,ω) mesons. The resulting potentials are usually referred to as "one-boson-exchange potentials" (OBEP), or "two-pion-exchange potentials" (TPEP) in the case of two-pion exchange. This description is only valid for the medium- and long-range parts of the potential ($\gtrsim 0.8$ fm). Individual contributions to the potential from each meson exchanged include spin-spin, tensor, spin-orbit, and isospin-dependent terms, where applicable. The sum of the contributions from all exchanged mesons gives the real potential $V(NN)=\sum_m V_m$, where V_m denotes the contribution of meson m, and $m=\{\pi,2\pi,\eta,\omega,\text{ etc.}\}$. The long-range part is mostly due to pion exchange, the pion being the lightest of the mesons. The short-range "hard-core" repulsion is due mainly to ω exchange.

The $N\bar{N}$ potential can be obtained from that of the NN system since the two only differ at the N-m-N ($\bar{N}$-m-$\bar{N}$) interaction vertices of the relevant Feynman diagrams. This introduces a factor G_m for each meson exchanged, where G_m is the G parity of meson m. This technique is commonly referred to as the "G-parity transformation.[10,11] The resulting $N\bar{N}$ potential can then be written as $V(N\bar{N})=\sum_m G_m V_m$. Contributions from mesons with odd G parity (π,ω,ϕ,δ) have opposite signs in the $\bar{N}N$ and NN cases. In particular, the strong, short-range NN repulsion due to ω exchange now becomes a strong, short-range attraction. The naive implication of this observation is that with such a strong attractive potential there should be many bound states in the $N\bar{N}$ system.

The other important observation involving the real part of the $N\bar{N}$ potential has to do with coherence properties among the different meson-exchange potentials. The two basic types of coherences are (i) all contributions to a particular component (V_m) are of the same sign and (ii) contributions to a particular type of potential (e.g., central, tensor, etc.) from many different mesons are of the same sign. The most important coherence effect in the $N\bar{N}$ system comes from the fact that the central, tensor, and quadratic spin-orbit forces are all fully coherent and attractive for isospin $I=0$ states with total spin $S=1$ (Ref. 10). To illustrate, as pointed out recently by Dover,[11] the observation that $\sigma(\bar{p}p)>\sigma(\bar{n}p)$ could signal the effect of tensor forces which are particularly strong and attractive[12] for $I=0$, $J=l\pm 1$ states. Such coherent tensor forces do not operate for $\bar{n}p$ since it has $I=1$, for which the total tensor potential is expected to be much weaker.

The previous discussion on the real part of the $N\bar{N}$ potential has some obvious limitations. First of all, it can only be as reliable as the NN potential from which it was derived. This is not serious, since there has been much progress in mapping out a detailed phase-shift analysis of NN scattering. Also, as in the NN case, the $N\bar{N}$ potential derived in this way is only valid for relative distances $r\gtrsim 0.8$ fm. For smaller distances the $N\bar{N}$ interaction is dominated by annihilation and the NN system can provide no guidance, since the annihilation mechanism has no counterpart in the NN interaction. In fact, the presence of annihilation masks the effects of the short-range $N\bar{N}$ real potential in order to complete the potential model for $N\bar{N}$, an absorptive potential must be added to the real part.

The first attempt at incorporating annihilation into the $N\bar{N}$ potential was made by Bryan and Phillips.[13] They used the OBEP of Bryan and Scott,[7] applied the G-parity transformation, and added a phenomenological, purely imaginary potential, which is independent of spin, isospin, and energy. The authors noted that the imaginary potential is very strong at short distances and greatly attenuates the wave functions there, acting somewhat like the NN repulsive core. Also, this attenuation suppresses the short-range forces in the real part of the potential and essentially eliminates sensitivity to them.

Subsequent improvements to the NN potentials, in particular due to the Paris group,[9] have evolved. Dover and Richard[14] (DR) introduced the G-parity transformed versions of this potential, along with a complex phenomenological spin, isospin, and energy-independent annihilation potential (model DR I). Several notable features emerged from this analysis. First, the addition of the real annihilation potential (V) enables one to reduce the value of the imaginary potential (W), as well as improve the quality of fits to cross-section data. The observation made by the authors is that V focuses the wave functions on the an-

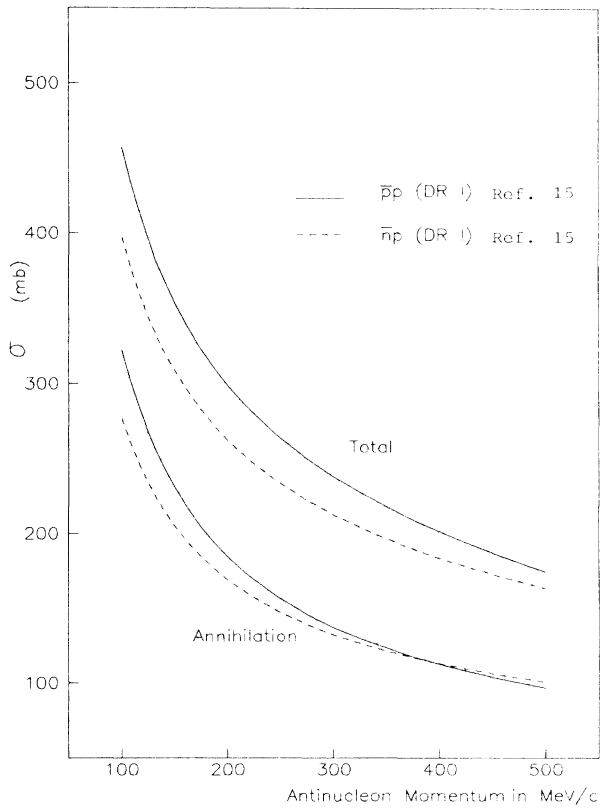

FIG. 1. $\bar{p}p$ and $\bar{n}p$ annihilation cross sections predicted by the DR I model (Ref. 15).

nihilation region. Therefore, the absorption strength can be reduced. Second, even though W is reduced, there is still considerable absorption at 1 fm.

Figure 1 shows a recent calculation by Dover[15] which compares $\bar{p}p$ with $\bar{n}p$ cross sections for model DR I at low energy. One sees that for both total and annihilation cross sections $\bar{p}p$ and $\bar{n}p$ differ, apart from annihilation above ~ 300 MeV/c. The sign of this difference is in agreement with the statement made previously regarding coherence in the isospin $I=0$ system.

The Paris group subsequently fit the available $\bar{p}p$ data, including angular and polarization distributions, and provided a much more flexible form for the annihilation potential.[16] This form has no real part as in the Dover and Richard model, but does include an explicit energy dependence. It was introduced to account for the fact that one expects more annihilation channels to open up with increased energy. Six parameters were adjusted to give the best fit to the data, and are different for isospin 0 and 1. The $I=0$ and $I=1$ forms of the potential W differ by up to 20% at very low energies ($E_{\rm lab}\simeq 0$), with $W(I=0)$ being larger. The effects at higher energies ($E_{\rm lab}\simeq 100$ MeV) are not as strong. Figure 2 shows the cross sections for $\bar{p}p$ and $\bar{n}p$ for the Paris model[16] in the energy region of interest here. It has characteristics similar to that of the DR I model discussed above.

Summarizing, the phenomenological potential models discussed here work reasonably well for describing $\bar{p}p$ cross-section data. They are able to predict some spin-isospin effects. In particular, because of coherence effects in the $I=0$ tensor force, $\sigma(\bar{p}p)$ is expected to be larger than $\sigma(\bar{n}p)$. This last point is of special interest to this experiment.

III. MICROSCOPIC MODELS

Recently there has been much work done on models motivated by quantum chromodynamics (QCD), in which the $N\bar{N}$ system is described in terms of quarks and gluons confined in bags. Several groups have considered annihilation channels resulting from quark annihilation or rearrangement graphs involving a nucleon ($3q$) and antinucleon ($3\bar{q}$). An especially well-presented recent summary of this work can be found in Ref. 17. In general, most available calculations have not yet addressed the question of isospin-dependent total and annihilation cross sections. However, we have recently been provided new calculations by the Helsinki and Tübingen groups, which will be discussed later in the context of our data.

IV. PREVIOUS EXPERIMENTAL SITUATION

There are no published data on $N\bar{N}$ total and annihilation cross sections below ~ 300 MeV/c momentum (1900 MeV). Virtually all of the published data above 1900 MeV are for $\bar{p}p$ cross sections only. A summary of the

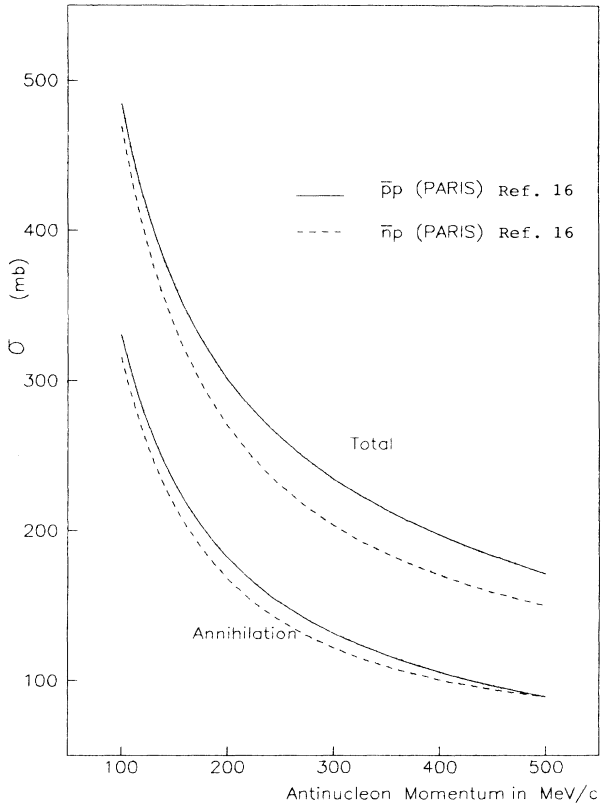

FIG. 2. $\bar{p}p$ and $\bar{n}p$ annihilation cross sections predicted by the Paris model (Ref. 16).

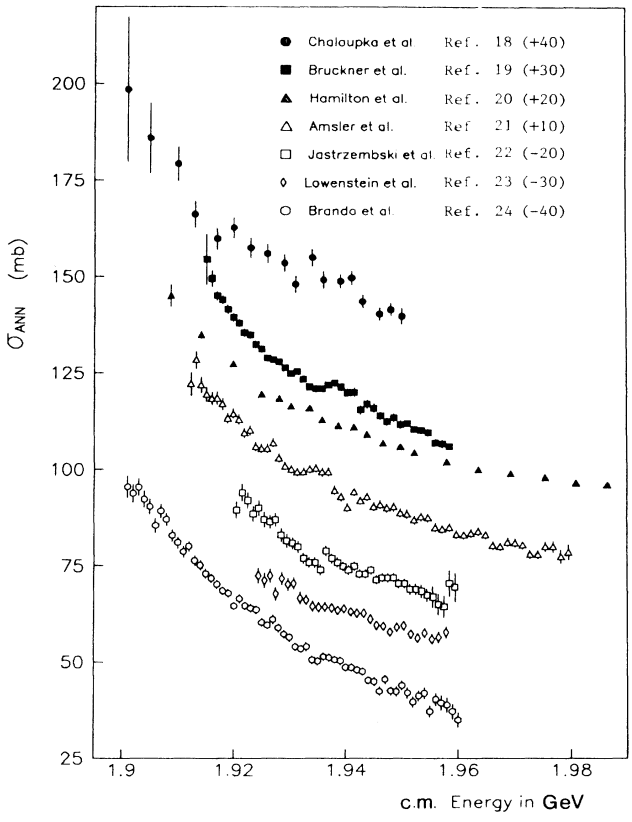

FIG. 3. Previously measured $\bar{p}p$ annihilation cross sections (Refs. 18–24). Each data set has been offset for clarity (e.g., + 40 mb).

present status of annihilation cross sections[18–24] is shown in Fig. 3. One should be cautioned that the experiments cited in Fig. 3 differed in geometry, triggers, etc., and hence did not necessarily measure the same quantity. The only $\bar{n}p$ annihilation cross-section measurement was performed by Gunderson *et al.*[1] Their data are shown in Fig. 4. As one can readily see, the errors are very large and could certainly mask all but the most dramatic effects. Another relevant measurement is that of Kalogeropoulos and Tzanakos.[2] They used a deuterium bubble chamber to measure $\bar{p}d$ annihilation cross sections, including the $\bar{p}p$ and $\bar{p}n$ components. Since the $\bar{p}n$ system is pure $I=1$, this reaction is identical to the $\bar{n}p$ reaction. Their results are also shown in Fig. 4. Finally, Balestra *et al.*[25] have measured the quantity $R=\sigma_{\text{tot}}(\bar{p}n)/\sigma_{\text{tot}}(\bar{p}p)$ based on an analysis of $\bar{p}$-neon data and Glauber theory. They report $R=0.76\pm0.06$ at 300 MeV/c, a value which agrees with other measurements in deuterium, helium, and carbon.

In summary, the paucity of published $\bar{n}p$ and $\bar{p}n$ data provides strong motivation for a careful study of total and annihilation cross sections over a broad momentum range. Good $p\bar{p}$ data, available only above 300 MeV/c, allow a comparison with $\bar{n}p$ data for the purpose of checking theoretical predictions discussed previously.

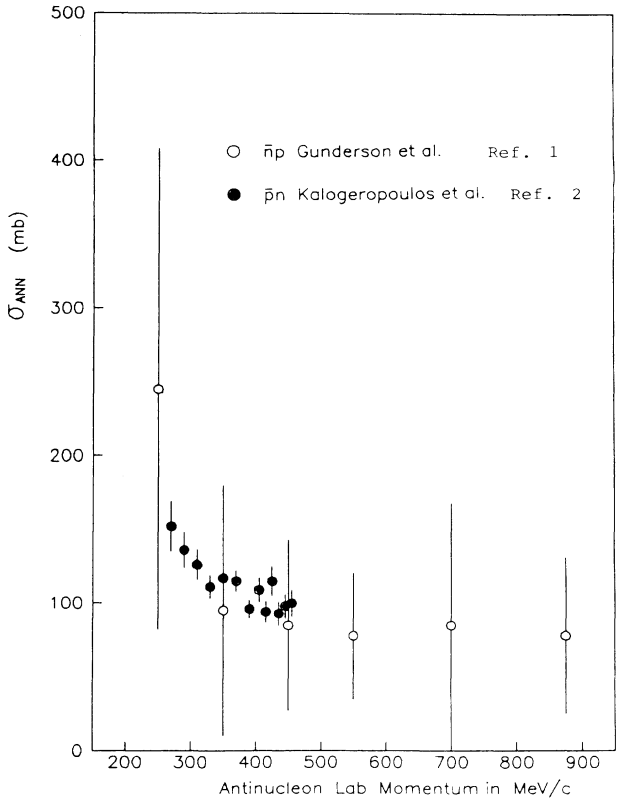

FIG. 4. Previously measured $\bar{n}p$ and $\bar{p}n$ annihilation cross sections (Ref. 12).

V. EXPERIMENTAL APPARATUS

The apparatus is shown in Fig. 5. The setup consisted of four basic components: (i) antiproton beam and identification; (ii) antineutron source; (iii) liquid-hydrogen target; and (iv) antineutron calorimeter. These components, along with their functions in the experiment, will be described in the following discussion.

A. Antiproton beam and identification

The experiment (E-767) was carried out in the C8 branch of the low-energy separated beam (LESB II) at the Brookhaven National Laboratory AGS. The charge-exchange mechanism ($\bar{p}p\rightarrow\bar{n}n$) was used to produce antineutrons. The beam was operated at transport momenta of 505 and 520 MeV/c. A lead collimator was installed to eliminate pions and muons which were not directly in the beam. However, contamination in the beam was about 200 π^-/p^-. At these momenta pions have roughly twice the velocity and one-fourth the energy loss of antiprotons. Using these facts, beam antiprotons were

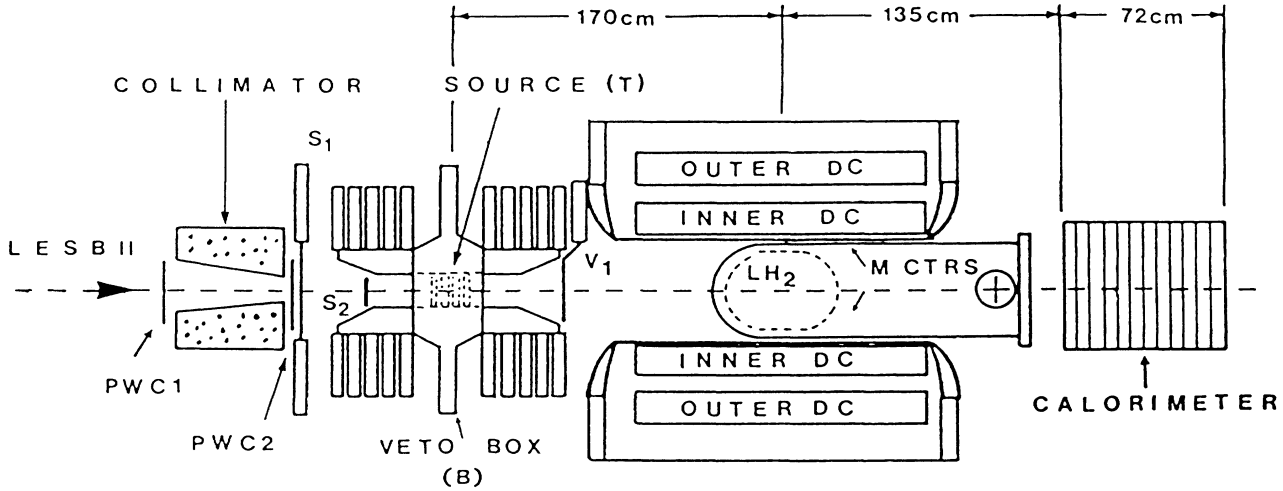

FIG. 5. Schematic plan view of the E-767 apparatus.

identified by time of flight (TOF) between counters BH and $S1$, as well as by their energy loss in counters $S1$ and $S2$. Here, BH (not shown in Fig. 5) is a hodoscope of ten counters, each $3\times25\times32$ mm^3, placed side by side in the beam 3.89 m upstream of counter $S1$. Figure 6 shows a TOF distribution, relative to the time at $S1$, for unnormalized samples of pions and antiprotons. The separation in time between them is about 13 ns, which is distinguishable by the trigger logic. In addition, a large energy loss ($\gtrsim 3\times$ minimum ionization) was required in counters $S1$ and $S2$. The trigger level logic for identifying an antiproton in the beam was

$$\bar{p}\equiv BH\cdot S1\cdot S2\cdot[\mathrm{TOF}(S1\text{-}BH)>20\ \mathrm{ns}]\cdot[\mathrm{PH}(S1)>3\times\ \mathrm{minimum}]\cdot[\mathrm{PH}(S2)>3\times\ \mathrm{minimum}]\ , \tag{1}$$

where PH$\equiv$signal pulse height, proportional to energy loss due to ionization in the counter, and minimum$\equiv$energy of minimum ionization. The beam intensity was typically 2500 $\bar{p}/s$ and 5×10^5 π^-/s. The pion rejection using this trigger was better than 10^5:1.

The incident antiprotons were tracked by two proportional wire chambers: PWC1 and PWC2. Each chamber was comprised of an x and y coordinate sense-wire plane with 2-mm wire spacing. The size of the beam at the focus (the antineutron "source") was 2 cm vertically and 10 cm horizontally.

The momentum spread of the beam was measured by calculating the antiproton momentum based on its TOF from BH to $S1$. This gave an rms spread of approximately 4%. This measurement is a superposition of the intrinsic momentum uncertainty of the beam and measurement errors associated with the time-and-flight path of the $\bar{p}$, and agrees well with that found from previous experiments using this beam line.[23,24]

B. Antineutron production

Antineutrons were produced by charge exchange of antiprotons in the source, which was comprised of 20 scintillation counters (T_1–T_{20}, or T counters) stacked along the beam direction. Its overall thickness was sufficient to degrade the antiproton energy so that they stopped close to the end of the stack. Each counter had dimensions of $0.6\times5\times13$ cm^3 and had timing and pulse-height information recorded for each event. It therefore acted as a source of antineutrons (from collisions on both carbon and hydrogen in the scintillator), as well as a detector for tracking antiprotons as they passed through it. The last counter hit provided information on the time and location

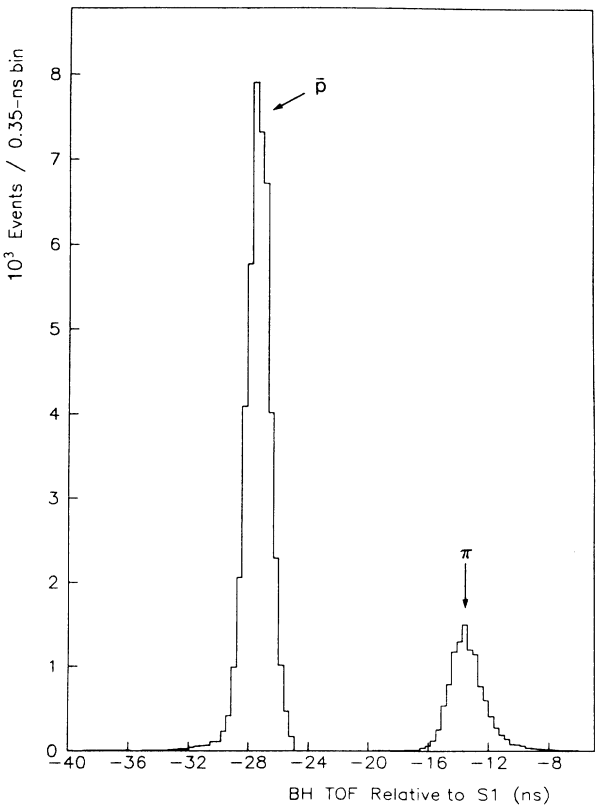

FIG. 6. Time-of-flight distribution for unnormalized samples of pions and antiprotons in the beam.

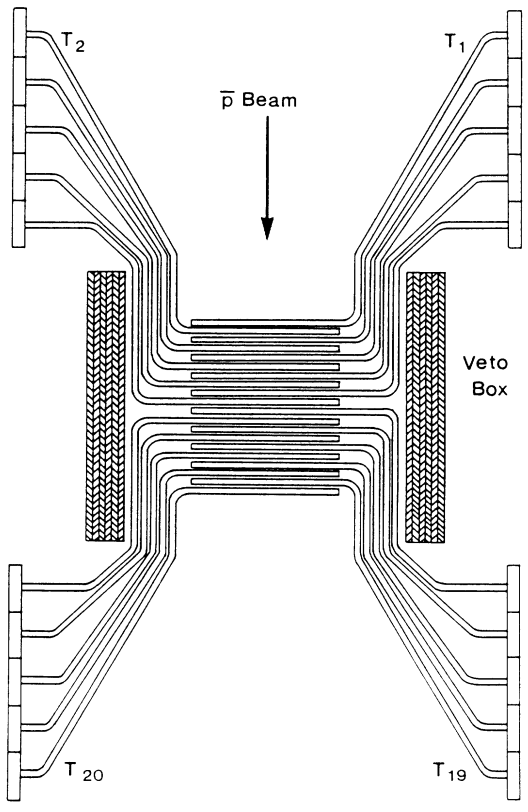

FIG. 7. Plan view of the antineutron source and veto box assembly.

of the antineutron production. This ultimately enabled the momentum of the $\bar{n}$ to be determined. A plan view of the source is shown in Fig. 7.

Since the momentum threshold for the charge-exchange reaction is 98 MeV/c, antineutrons can only be produced by antiprotons in flight. About 2% of the incident antiprotons produce antineutrons, while the remainder annihilate either in flight or at rest. In order to reject these annihilation events a veto system was arranged around the source on four sides ("veto box," B_1–B_{12}). A section of two sides of the box is seen in Fig. 7. Each side was oriented parallel to the beam direction and consisted of three layers of lead and scintillator, each for identifying charged particles and γ rays. The efficiency of the system for rejecting annihilation events was measured by examining antiprotons which interact in the source. The efficiency was determined to be greater than 98% by comparing the number of such events which give more than one hit in the veto box to the total number of annihilations.

If an event contained more than one veto box hit it was rejected as being a nonantineutron event. One hit was allowed to compensate for interaction of the neutron from charge exchange. The trigger logic for an antineutron trigger was $\bar{n} \equiv \bar{p} \cdot (\sum B < 2)$. Just downstream of the source was an additional veto counter ($V1$), which was used to reject events associated with beam pion accidentals.

C. Hydrogen target

Further downstream (170 cm) of the antineutron source was a cylindrical liquid-hydrogen (LH) target (Fig. 5). The hydrogen target flask was a cylinder 35 cm long with a diameter of 40 cm. The cylinder was closed on each end by spherical caps of radius 30.5 cm. The longest dimension of the target was 50 cm. The walls of the cylinder (end caps) were 0.10 (0.08) cm of Mylar. The flask was wrapped in 60 layers of superinsulation, with a total thickness equivalent to 0.04 cm of Mylar.

The vacuum vessel consisted of a 0.32-cm-thick aluminum cylinder with a 50.5 cm diameter. The upstream dome had a radius of 24.6 cm and was 0.16 cm thick. The overall length of the vessel was 149.9 cm. The downstream window was 0.019 cm thick, surrounded by a 2.54-cm-thick flange of 58.4 (54.6) cm outer (inner) diameter. Surrounding the vacuum vessel were 12 counters (M) in a barrel stave arrangement.

D. Calorimeter

The antineutrons were detected in a calorimeter 135 cm downstream of the LH target. Figure 8 shows a schematic isometric view of the calorimeter. It consisted of twelve modules, each module containing two (x,y) planes of aluminum proportional drift tubes, a four-element scintillator hodoscope (x or y), and a 2-cm-thick aluminum plate absorber in all but the first three modules. The mass of the first three modules was decreased to allow low-energy antineutrons to penetrate further into the detector before annihilating, where they had a better chance of being identified. Each drift tube plane consisted of 48 individual cylindrical tubes of length 61 cm, outer diameter 1.27 cm, and wall thickness 0.4 (0.9) mm in modules 1–3 (4–12). Each tube had a 25-μm-diameter gold-plated tungsten sense wire strung along its axis under 50 g of tension. The gas used was an 80% argon, 20% CO_2 mixture. The operating voltage of the sense wires was ~ 1600 V, while the tube walls were at ground potential. In addition, adjacent tubes were ganged together electronically. This gave a total of 576 channels available for track detection. The total equivalent length of aluminum along the beam direction was about 28 cm. The 48 scintillation counters (C_1–C_{48}) had cross-sectional dimensions 15×61 cm^2 and thickness 0.6 (1.3) cm in modules 1–3 (4–12). Every other module was rotated 90° to minimize systematic cracks in the detector.

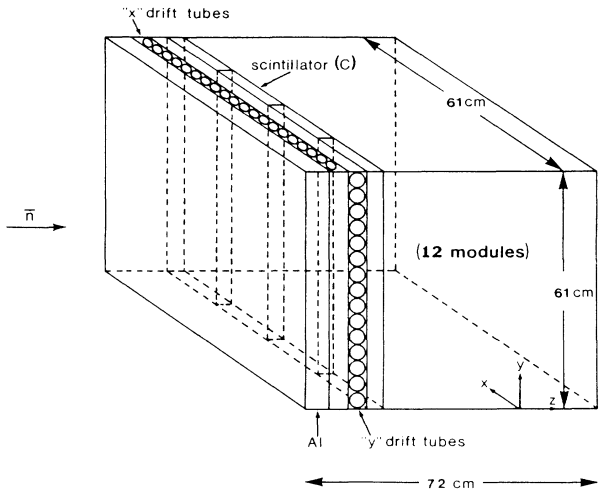

FIG. 8. Schematic isometric view of the antineutron calorimeter.

The drift tubes provided basic yes/no information on charged particles passing through them. These hits were used to locate an approximate vertex (within ± 5 cm), limited by the detector granularity and multiple Coulomb scattering. Because of the long $\bar{n}$ flight path (~ 350 cm) this accuracy was sufficient for a good TOF measurement.

The C counters had time and pulse-height information read out for each event. When correlated with the vertex location, the counter times could be adjusted to give the time at the annihilation point, and hence the $\bar{n}$ momentum by TOF.

E. Data acquisition

Data were collected by an on-line CAMAC data-acquisition system and a DEC PDP 11/34 minicomputer. Data collection was begun at 520 MeV/c incident $\bar{p}$ momentum, but was subsequently changed to 505 MeV/c since about 10% of the $\bar{p}$'s were penetrating the source because of the momentum spread in the beam. Approximately one-third of the data were taken at the 520-MeV/c setting. Data were collected in approximately equal amounts with target full and empty conditions. A total of $\sim 2 \times 10^6$ triggers were acquired and analyzed.

VI. DATA ANALYSIS

Cross sections were measured by the "transmission" method, which involved measuring the antineutron flux in the calorimeter with the target full and empty. The ratio of these yields, normalized to the total beam exposure for each, is directly related to the total and annihilation cross sections. Furthermore, since the calorimeter was used to measure both yields, corrections due to inefficiences related to the calorimeter cancel out in this ratio. This greatly reduced sources of systematic error in the absolute cross-section determination.

A. Counter calibrations

Calibration of the time and pulse-height information from all scintillators was done with beam pions. The velocity spread of these pions was negligible despite the large momentum spread of the beam. Since the beam pions used in the timing calibration were minimum ionizing particles, they were also used to calibrate the pulse heights. This was done by calculating a "gain" factor which normalized the observed pulse height of minimum ionization energy to 100 units.

B. Antineutron identification in the source

The conditions required to identify an antineutron produced by charge exchange in the source began with identifying an incoming antiproton, described earlier. The source T counters were then examined. In general, a $\bar{p}$ interaction in the source had the characteristics of large pulse heights (>200 units) in successive T counters up to some counter T_n, and then either no subsequent hits (charge exchange), or subsequent hits with low pulse heights (<200 units) from annihilation secondaries. An interaction profile, defined as the distribution of counters in which the p disappears, is shown in Fig. 9. The large peak centered at T_{16} corresponds to $\bar{p}$ annihilations at rest.

The signature of a charged-exchange event in the source corresponded to having no subsequent T counters fire after the $\bar{p}$ disappeared. In addition, it was required that there be no veto box hits with times correlated with the incoming $\bar{p}$. As mentioned previously, the hardware trigger did allow for a single veto box hit in case the neutron from charge exchange fired one of the counters. However, it was found that events with this topology were also produced by various background mechanisms, and the condition $\sum B=0$ was rigorously imposed off line. Finally, the downstream veto counter $V1$ was examined for a hit. If this counter had a very large pulse height (>350 units) or had timing consistent with the incoming $\bar{p}$, the event was rejected. The large pulse height was used to eliminate events in which the $\bar{p}$ penetrated the source. Figure 10 shows the profile of charge-exchange events in the source. The rapid fall-off of events toward the down-

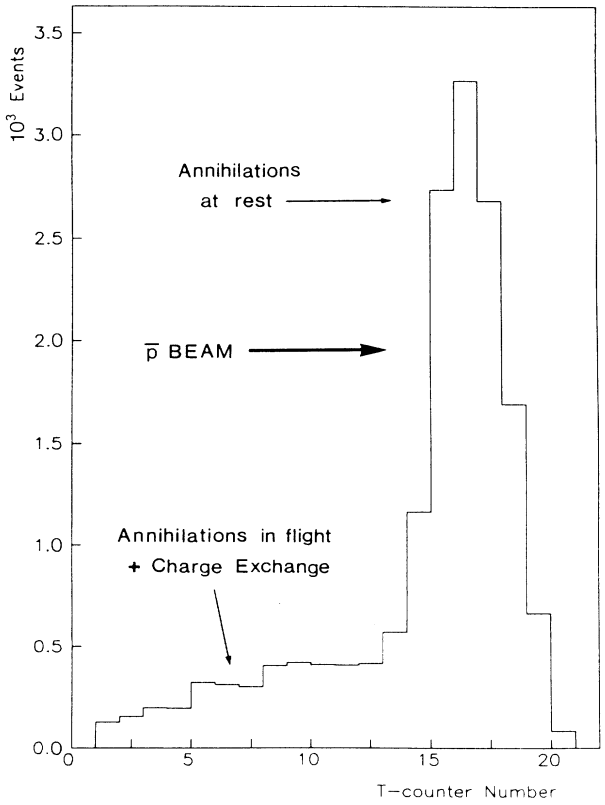

FIG. 9. Antiproton annihilation profile in the antineutron source.

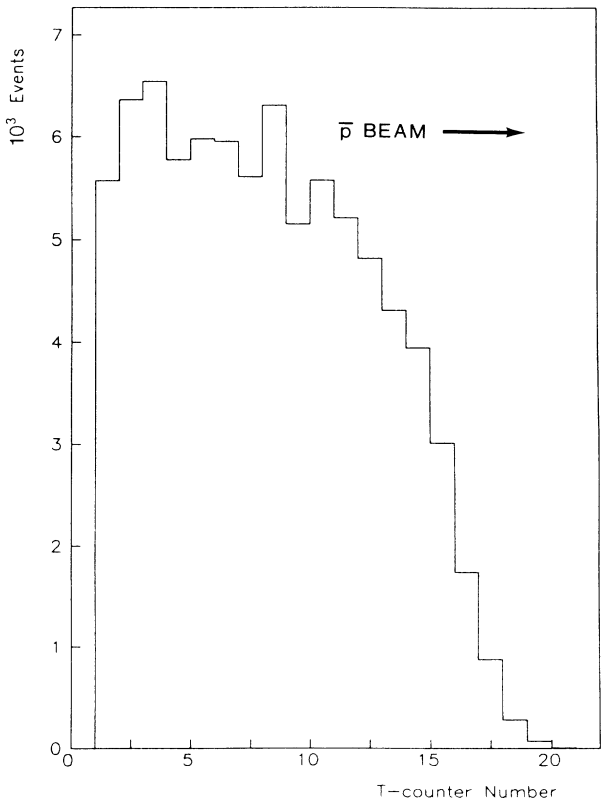

FIG. 10. Profile of charge-exchange events in the antineutron source.

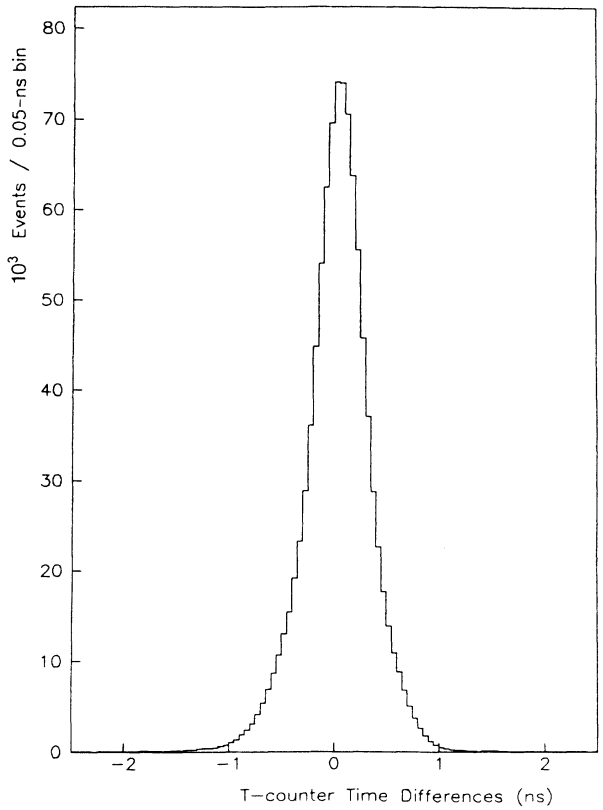

FIG. 11. Time difference between all pairs of counters hit in the antineutron source.

stream end of the source is due to the attenuation of antiprotons stopping in the source.

The time for the $\bar{n}$ production in the source was obtained by averaging the times for T_n and T_{n-1} $(n>1)$. The error in the T-counter times was measured by examining time differences between all possible pairs of counters that were hit, corrected for the $\bar{p}$ flight time between them. These differences are plotted in Fig. 11. The rms width of this distribution is a measure of the timing error for a pair of counters, and was found to be 0.16 ns per counter. The position of the $\bar{n}$ production was assumed to be at the center of the counter. The error in the position is at most half the counter thickness, or 0.3 cm.

C. Calorimeter event analysis

Calorimeter (CA) events were defined at the trigger level as

$$\mathrm{CA}\equiv\bar{n}\cdot\left[\sum C>0\right]\cdot\overline{[\mathrm{TOF}(V1\text{-}C)<10\ \mathrm{ns}]}\ , \tag{2}$$

where the TOF requirement rejected events in which a beam pion triggered the system.

1. Time and vertex reconstruction

The algorithm required to locate the $\bar{n}$ annihilation vertex relied solely on drift-tube hit information. Drift-tube planes were oriented in x,y pairs approximately every 6 cm along the beam direction. The effective spacing between wires in a plane was 2.5 cm since adjacent wires were ganged together electronically. An initial guess at the vertex location was made by averaging the coordinates of the hits. After determining this initial trial vertex, the hits were decoupled into two two-dimensional views, x-z and y-z, where the z coordinate is along the beam direction. In each view, the area around the trial vertex was divided into grids. The center of each grid would then in turn be tried as a trial vertex. Emanating from each of these trial vertices, tracks were constructed at discrete angular steps, initially 45°. For each of these trial tracks, a quality parameter was calculated which measured how well the wire hits lined up with the track.

The general form for this parameter was

$$C_{ijk}=\sum_{n}^{N_k}(d_n{}^2+a^2)^{-1}(r_n{}^2+b^2)^{-1}\ , \tag{3}$$

where i, j, k, and n are track, grid, view, and wire hit indices, respectively, N_k is the number of hits in that view, d is the perpendicular distance from the hit to the track, r is the radial distance from the trial vertex to the hit, and a,b are adjustable parameters. The first factor measures the closeness of the hits to the trial track, and the parameter C_{ijk} increases as d decreases. The second factor ensures that less weight is given to a hit that is far away from the vertex and served to localized the vertex search. In each view, the grids corresponding to the two largest

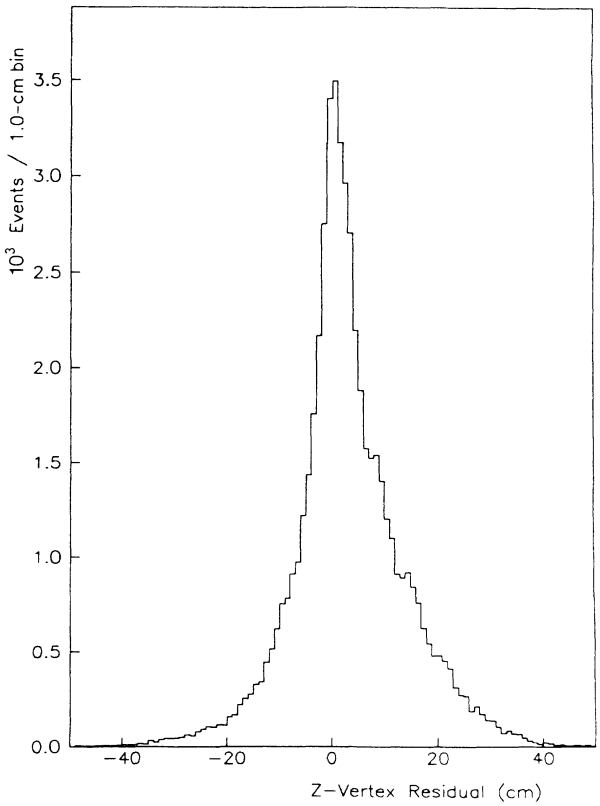

FIG. 12. z-coordinate vertex residuals in the calorimeter.

C_{ijk} were averaged to give a new vertex location, which was then used as the initial vertex for the next iteration of the algorithm. This whole process was iterated a total of three more times using increasingly smaller grid sizes and angular steps. The resulting final vertex was taken as the annihilation point.

The accuracy of the vertex algorithm was measured using a detailed Monte Carlo simulation of annihilations in the calorimeter. Events from this simulation were fed into the analysis program and the resulting vertex was compared to the (known) annihilation point. Figure 12 shows the difference (residual) in the z coordinates of the two. The z-coordinate resolution dominates the uncertainty in the flight path of the antineutron. The rms width of the distribution is ~ 5 cm, and is a measure of the position resolution in the calorimeter.

The annihilation time was obtained from C-counter information. For each counter hit in a event, nearby drift tube hits were used to reconstruct the hit location. This information was used to make corrections to the counter time. The first was to correct for variations in transit TOF in the scintillator. Because of the large size of the counters (61×15 cm^2), this correction could be up to 2 ns for a given counter. The second correction involved the distance from the calculated vertex to the counter hit location. Using a secondary particle velocity of $0.9c$, the TOF between the vertex and the counter was calculated and subtracted from the observed time. This adjustment could be up to 3 ns. With the addition of these corrections, the time at the annihilation point was obtained as the average of the counter times in an event. Figure 13 shows the distribution of time differences between all pairs of counters hit for selected annihilation events. This measured how well the counters agreed on the annihilation time, and its width is consistent with a single counter rms resolution of 0.39 ns.

Given the time and location of the $\bar{n}$ annihilation in the calorimeter, and similar information on its production in the source, the momentum (and associated errors) of the antineutron were calculated. The resultant uncertainty in the $\bar{n}p$ c.m. mass determination is plotted in Fig. 14. We note that above 1900 MeV (300 MeV/c) these errors are comparable to typical values from previous $\bar{p}p$ measurements,[16–22] and below 1900 MeV reach as low as ~ 100 keV, values far superior to those achieved before in $\bar{N}N$ formation measurements. This result has been exploited to great advantage in the search for narrow states.[3]

2. *Antineutron identification in the calorimeter*

The large rate of pions ($\sim 5 \times 10^5$ π^-/s) coupled with the long event sampling time (~ 100 ns) in the calorimeter lead to an appreciable number of CA triggers due to pion accidentals. To eliminate this background, the following set of software criteria were devised. The first criterion was a charge-exchange signature in the source/veto box as

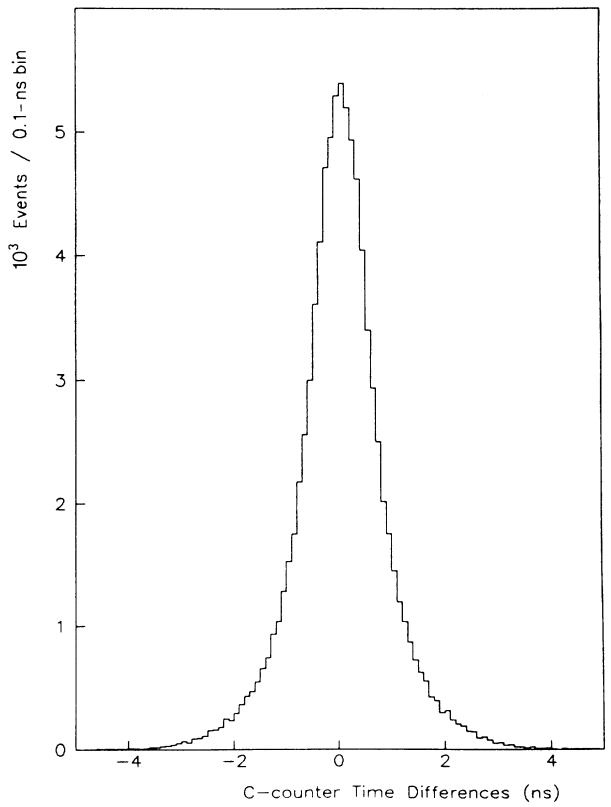

FIG. 13. Time difference between all pairs of C counters hit in an event.

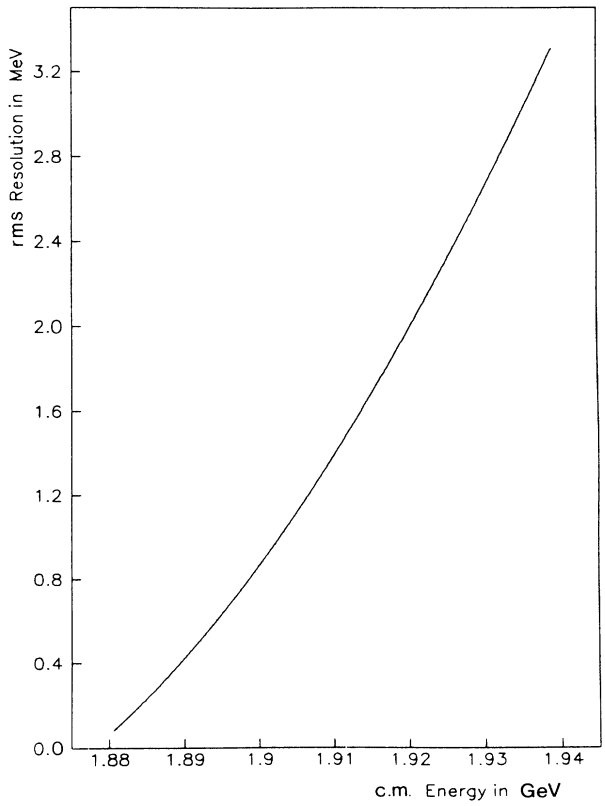

FIG. 14. rms mass resolution for calorimeter events.

defined previously. Next, a lower limit was placed on the amount of energy deposited in the C counters for an event. Specifically, the normalized pulse heights of all counters were summed ($\sum_c$) and required to be larger than the equivalent of twenty minimum-ionizing particles (2000 units). This limit stemmed from observations on how pions behaved in the calorimeter. In general, they leave behind drift tube hits which lie in a straight line and hit one C counter in each module. Since they are minimum ionizing particles, they deposit on the average 1200 units of energy. This is shown in Fig. 15, where $\sum_c$ is plotted for known pion events. The high-energy tail in the distribution is due to Landau fluctuations in the energy loss plus interactions in the counters. The peak at zero in $\sum_c$ is attributed to pions interacting in the source and target, producing neutrons and photons which deposit a small amount of energy in the calorimeter. A cut at 20 minimum ionizing (2000 units) was sufficient to eliminate 91% of the pions.

As a further criterion, a straight-line fit was made to all hits from the drift tubes. A pion track should give a good χ^2 (G_f) for this hypothesis, while an annihilation event will not. Figure 16 shows the distribution of G_f for known pion events. The requirement $G_f > 3$ eliminated 92% of these events. The overall effect of the $\sum_c$ and G_f requirements on pion events can be seen in the scatter plot of Fig. 17, where only 4% of the tracks pass both cuts.

We can estimate an upper limit on beam pion-induced

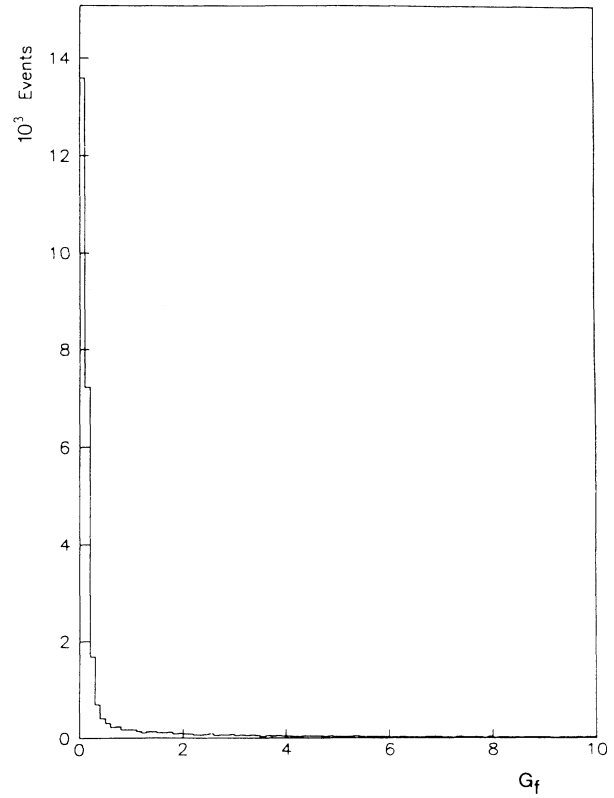

FIG. 16. G_f distribution for beam pions in the calorimeter.

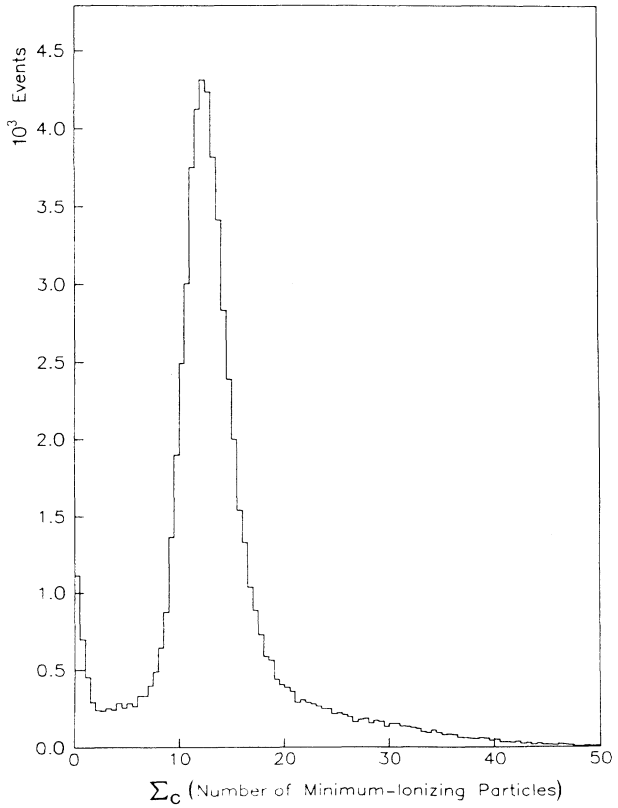

FIG. 15. Pulse-height sum ($\sum_c$) for beam pions in the calorimeter.

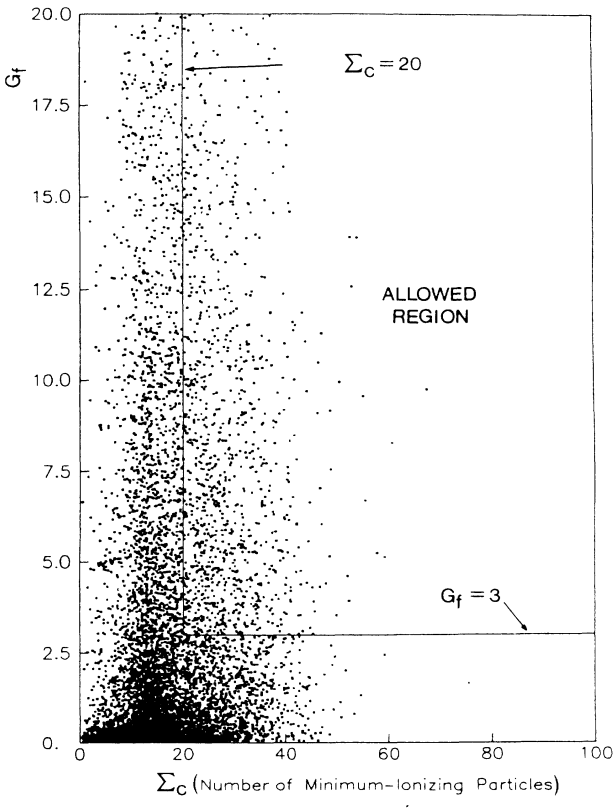

FIG. 17. G_f vs $\sum_c$ for beam pions in the calorimeter.

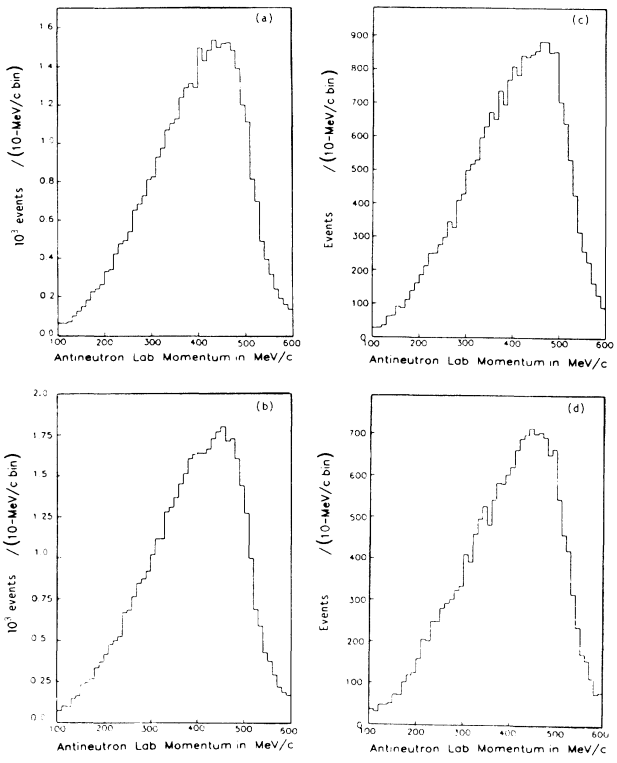

FIG. 18. (a) Uncorrected CA (target full) yield (505 MeV/c); (b) uncorrected CA (target empty) yield (505 MeV/c); (c) uncorrected CA (target full) yield (520 MeV/c); (d) uncorrected CA (target empty) yield (520 MeV/c).

contamination in the antineutron event sample. A CA trigger would be formed by an accidental pion during the 100-ns gate interval which followed a charge exchange in the source. The observed charge-exchange rate was 30/s. Assuming a lower-limit efficiency of 99%, this give a upper limit on the pion-induced event rate of $(5\times10^5\ \pi^-/\text{s})\times(10^{-7}\ \text{s})\times(30/\text{s})\times10^{-2}=0.015/\text{s}$. Applying the $\sum_c/G_f$ cut described above, the limit becomes 6×10^{-4}/s, to be compared with a final $\bar{n}$ events rate of 0.2/s. We conclude that pion accidental background in the final event sample is negligible.

Antineutron events selected by the above criteria were then plotted as momentum distributions for both target empty and target full data (Fig. 18), from which cross section distributions were obtained as discussed below.

3. *Corrections to calorimeter yields*

First, a correction factor (ϵ_t) was needed for the CA (target full) data to account for antineutrons which hit the calorimeter but did not traverse the full length of the target because of the finite radius of the target. Numerical values for ϵ_t are given in Table I. Details may be found in the Appendix. These corrections are on the average 7% and insensitive to momentum.

Second, a correction factor was required to account for elastic scatters in hydrogen. Because of the finite size of the calorimeter and its distance from the LH target, about 82% of the antineutrons which elastically scattered in the hydrogen subsequently missed the calorimeter. Therefore, in order to measure the total (annihilation) cross section by the transmission method, elastically scattered antineutrons which hit (miss) the calorimeter had to be taken into account. The total cross section is corrected by subtracting away the scattered antineutrons which subsequently hit the calorimeter. This correction (ϵ_s^T) is described in the Appendix and given in Table II. It is 3% on the average and insensitive to momentum.

The major source of background is antineutrons which elastically scatter into the calorimeter from material surrounding the target and from the walls and floor. Such events would be characterized by longer TOF's as compared to direct antineutrons. Also, antineutrons which annihilate outside the calorimeter may send pions and γ rays into the calorimeter. Such events are largely suppressed by cuts on G_f and $\sum_c$, as well as TOF ($M<$CA). The latter cut removes those antineutrons which annihilate near the target and send pions into both the M counters and the calorimeter.

The most serious background comes from antineutrons which scatter or annihilate in material near the target. We have experimentally estimated such background by comparing normal target empty calorimeter yields with the yield obtained with the target, M counters, drift chambers, and their support structure removed. From

TABLE I. Target length correction factors to be applied to CA (target full) yields. The error is statistical only. See the Appendix for details.

Momentum (GeV/c)	ϵ_t
0.125	0.882±0.022
0.175	0.920±0.013
0.225	0.939±0.011
0.275	0.936±0.009
0.325	0.947±0.007
0.375	0.954±0.006
0.425	0.959±0.005
0.475	0.967±0.006

TABLE II. Correction factors to be applied to CA (target full) yields due to elastic scattering in the hydrogen. The first error is statistical, the second systematic. See the Appendix for details.

Momentum (GeV/c)	ϵ_s^T
0.125	0.983±0.008±0.01
0.175	0.985±0.004±0.01
0.225	0.975±0.004±0.01
0.275	0.982±0.003±0.01
0.325	0.982±0.003±0.01
0.375	0.977±0.003±0.01
0.425	0.967±0.003±0.01
0.475	0.970±0.003±0.01

TABLE III. Ratio of antineutrons scattered from materials which surround the target to antineutrons directly from the source (β/Y_e).

Momentum (GeV/c)	β/Y_e
0.125	0.196±0.098
0.175	0.166±0.083
0.225	0.137±0.068
0.275	0.109±0.054
0.325	0.083±0.042
0.375	0.058±0.029
0.425	0.034±0.017
0.475	0.011±0.005

these data we find the ratio of scattered to direct antineutrons varies from a maximum of (20±10)% (100 MeV/c) down to 0% (500 MeV/c). Values of this ratio are given in Table III. The data are corrected for this background as explained in the next section. The remaining, unmeasured background from antineutron scattering and annihilations in the floor and walls were crudely estimated from Monte Carlo calculations. These were found to be about 10% at 100 MeV/c and decrease rapidly to 0% at 350 MeV/c. Since this correction is poorly known, but appears to be within the error bars already applied, it was not taken into account.

VII. METHOD OF CROSS-SECTION CALCULATIONS

This section gives details on the actual formalism used in obtaining cross sections from the transmission method. Since data were taken at two different beam momenta, the expressions given here were applied to each data set, which were than combined and weighted according to statistical error.

The total cross section (σ_T) is given by

$$\sigma_T(p)=\sigma_0 \ln[I_0(p)/I_t(p)] \ , \quad \sigma_0=m/\rho L=480\pm 6 \text{ mb} \ , \tag{4}$$

where I_0 is the incident antineutron intensity, I_t is the transmitted intensity, m is the proton mass, ρ is the density of hydrogen (0.070 g/cm^3), and L is the maximum target length (50 cm). The error in σ_0 arises from uncertainties in both the density and target length. The quantities I_0 and I_t are given by

$$I_0(p)=Y_e(p)/n_e-\beta(p) \ , \tag{5}$$

and

$$I_t(p)=Y_f(p)\epsilon_s^T(p)\epsilon_t(p)/n_f-\beta(p) \ , \tag{6}$$

where $Y_e(p)$ and $Y_f(p)$ are the yields of antineutrons detected in the calorimeter for target empty and full, respectively, n_e and n_f are the numbers of antiprotons incident on the source for target empty and full, respectively, and $\beta(p)$ is a correction for antineutrons which scatter into the calorimeter from materials which surround the target. A summary of the Y and n data integrated over p is given in Table IV. The annihilation cross section can be obtained by simply subtracting the elastic cross section (see the Appendix) from σ_T.

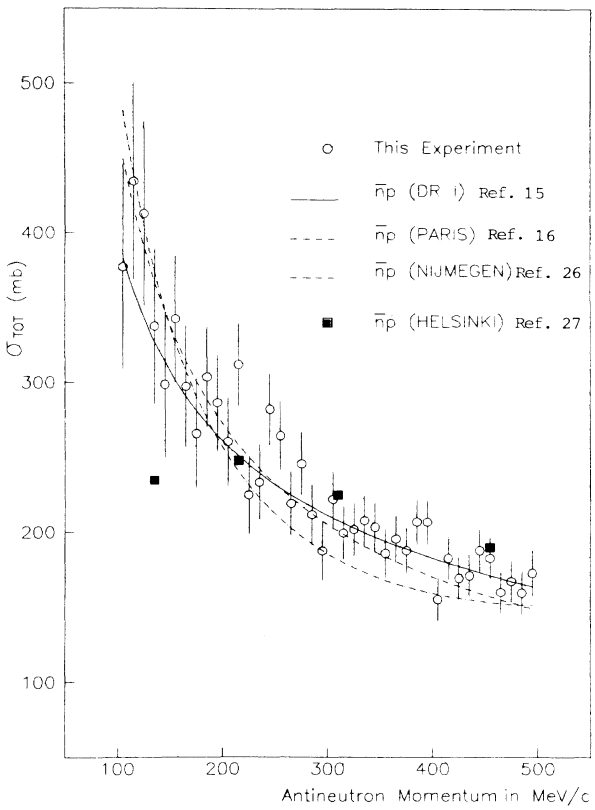

FIG. 19. Total cross sections as measured by this experiment, compared with theoretical model predictions from Refs. 15, 16, 26, and 27.

VIII. FINAL CROSS SECTIONS AND DISCUSSION

Annihilation cross sections are given in Table V. Using the simple parametrization form ($A+B/p$), an excellent fit (χ^2/DF=29/38) was obtained with $A=41.4\pm 9.0$ mb and $B=29.0\pm 2.9$ mb GeV/c. The total cross sections are also given in Table V and plotted in Fig. 19. Again, an excellent fit (χ^2/DF=29/38) was obtained using the form

TABLE IV. Antineutron calorimeter yields and antiproton normalization factors.

Data type	Event data yield (Y)	Antiprotons (n)
505 MeV/c CA Empty	38 840	3.962×10^8
505 MeV/c CA Full	32 668	4.500×10^8
520 MeV/c CA Empty	15 131	1.453×10^8
520 MeV/c CA Full	18 568	2.461×10^8

TABLE V. Antineutron-proton cross sections as measured in this experiment. The first error is statistical, the second systematic.

Momentum (MeV/c)	σ_{ann} (mb)	σ_{tot} (mb)
105	258±68±65	377±68±65
115	321±66±57	435±66±57
125	304±62±50	413±62±60
135	233±52±45	338±52±45
145	197±48±40	298±48±40
155	244±42±37	342±42±37
165	202±40±33	297±40±33
175	173±36±30	266±36±30
185	213±34±29	304±34±29
195	198±32±26	287±32±26
205	174±29±24	261±29±24
215	226±28±23	312±28±23
225	141±26±21	225±26±21
235	151±25±19	233±25±19
245	200±24±18	282±24±18
255	184±23±17	265±23±17
265	140±21±16	220±21±16
275	167±21±15	246±21±15
285	134±20±14	212±20±14
295	111±19±13	188±19±13
305	147±18±12	222±18±12
315	125±18±11	200±18±11
325	128±17±11	202±17±11
335	134±16±10	208±16±10
345	130±16±10	204±16±10
355	113±16± 9	186±16± 9
365	124±16± 9	196±16± 9
375	116±15± 8	188±15± 8
385	136±15± 8	207±15± 8
395	137±15± 8	207±15± 8
405	85±14± 6	155±14± 6
415	113±14± 6	183±14± 6
425	100±14± 6	169±14± 6
435	102±14± 6	171±14± 6
445	119±14± 6	188±14± 6
455	115±14± 5	183±14± 5
465	92±14± 5	160±14± 5
475	99±14± 5	167±14± 5
485	92±14± 5	159±14± 5
495	105±15± 5	172±15± 5

$A+B/p$, with $A=94.4\pm9.0$ mb and $B=36.0\pm2.9$ mb GeV/c.

Comparison of the annihilation cross sections with previous $\bar{n}p$ (Ref. 1) and $\bar{p}n$ (Ref. 2) measurements have been made. In the former case, the large error bars preclude a meaningful quantitative comparison, although the data are obviously in good agreement. In the latter case, we have fit the E-767 (Ref. 2) values to the form of $A+B/p$ in the region of overlap (270–455 MeV/c) with the following results: $A=51\pm25$ (27 ± 17) mb, $B=26\pm9$ (30 ± 6) mb GeV/c, respectively. We note a 1–2-standard-deviation difference in A. However, after taking into account systematic errors (see Table V) which were not included in these fits, we conclude that this difference is not significant.

Figure 19 compares the $\bar{n}p$ total cross sections with predictions from four models. The χ^2/point values for the DR I, Paris, and Nijmegen[26] potential models are 33/40, 48/40, and 88/40, respectively, indicating a clear preference for the DR I model, although the Paris model cannot be ruled out. The Helsinki microscopic model[27] gives the least satisfactory comparison with the data of all four models. The flattening of the cross section below $\sim$200 MeV/c is due to the decrease in the P-wave contribution at low momenta.[27] Above $\sim$250 MeV/c the model is also too high. The Helsinki group notes that this may be due to insufficient repulsion, which would decrease in the $I=1$ wave function and, hence, the cross section.[27] We have recently received a microscopic model calculation from the Tübingen group.[28] At 500 MeV/c it reproduced only about 30% of the total cross section compared with our measurement. The authors note that this discrepancy may be due to the relative amount of three-meson quark rearrangement to two-meson quark annihilation processes assumed in their calculation.

We next compare our $\bar{n}p$ cross sections with previous $\bar{p}p$ measurements. In Fig. 20 we show E-767 annihilation cross sections with $\bar{p}p$ values from Ref. 24. This particular data set has been chosen among all of those displayed in Fig. 3 because it overlaps in momentum with the E-767 measurements and has good statistics (on these grounds the data of Ref. 18 were not selected). In the limited range over which the comparison can be made, the $\bar{p}p$

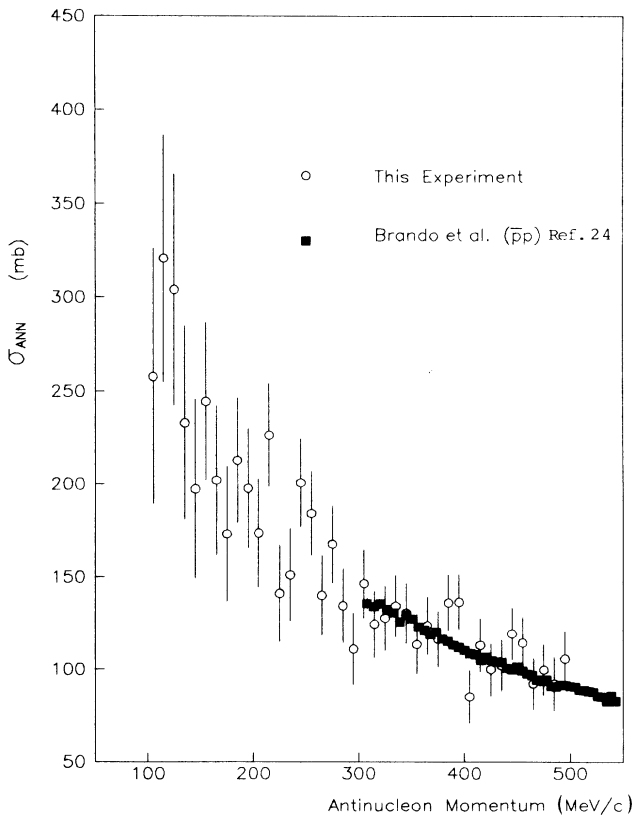

FIG. 20. Comparison of $\bar{n}p$ annihilation cross sections with $\bar{p}p$ data from Ref. 24.

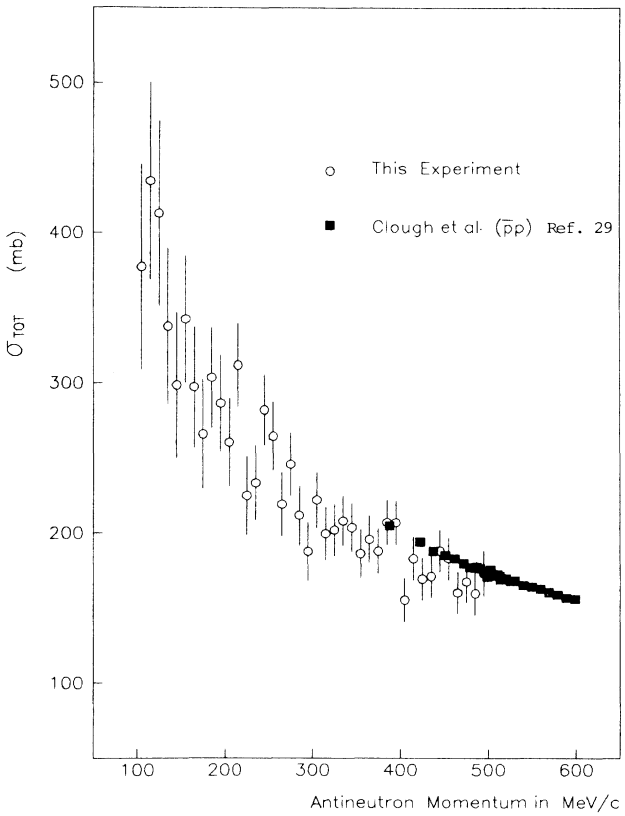

FIG. 21. Comparison of $\bar{n}p$ total cross sections with $\bar{p}p$ data from Ref. 29.

data are in excellent agreement with the $\bar{n}p$ data. We note that this is consistent with the predictions of the DR I (Fig. 1) and Paris (Fig. 2) models in this momentum region.

In Fig. 21 we show E-767 total cross sections with $\bar{p}p$ values from Ref. 29 which quotes exceptionally small statistical ($\pm 0.4\%$) and systematic ($\pm 0.7\%$) errors. Here we see the $\bar{p}p$ values are systematically larger (~ 20 mb) than the $\bar{n}p$ values. Again, in the limited range over which the comparison can be made, this result is consistent with the predictions of the DR I (Fig. 1) and Paris (Fig. 2) models, which show differences of ~ 15 and 30 mb, respectively. As new data become available at lower momenta it will be interesting to see if these observations in both our annihilation and total-cross-section data continue. Finally, from these data we find $R=\sigma_{\rm tot}(\bar{n}p)/\sigma_{\rm tot}(\bar{p}p)=0.84\pm 0.07 \pm 0.05$ at 300 MeV/c, where we have extrapolated the data of Clough *et al.*[29] to a value of ~ 245 mb at 300 MeV/c. This value is in good agreement with 0.76 ± 0.06 given by Balestra *et al.*,[25] based on $\bar{p}$-neon data and Glauber theory.

ACKNOWLEDGMENTS

The authors wish to express their appreciation to the AGS staff, and especially D. Lazarus and R. Meier. Discussions with C. Dover on the interpretation of the data have been particularly helpful. The work at Brookhaven was supported by the U.S. Department of Energy. The work at the University of Houston and Rice was supported in part by the U.S. Department of Energy. The work at Pennsylvania State was supported in part by the U.S. National Science Foundation.

APPENDIX: SIMULATION OF ANTINEUTRON INTERACTIONS IN THE LIQUID-HYDROGEN TARGET

In order to obtain corrections to the data involving the finite geometry of the target and elastic scattering in the target, a Monte Carlo simulation was performed.

Antineutrons were generated in the source from charge exchange of an incoming $\bar{p}$ beam with transport momentum 520 MeV/c and 4% rms spread. Charge-exchange cross sections were obtained from Ref. 30. From kinematics, the $\bar{n}$ momentum and trajectory was calculated and used to project it toward the hydrogen target. If the $\bar{n}$ entered the target, it was propagated through the hydrogen and allowed to interact. If the $\bar{n}$ survived the hydrogen, it was then projected to the calorimeter.

Antineutron-proton interaction probabilities in the momentum range 100–500 MeV/c were determined from cross sections obtained from the optical potential model of Ref. 14. The annihilation, elastic, and differential elastic cross sections were parametrized in the following forms: $\sigma_A({\rm mb})=58+22/p$, $\sigma_E({\rm mb})=53+7/p$, and $d\sigma_E/dt({\rm mb/GeV^2})=A\exp(bt)$, where p is the $\bar{n}$ laboratory momentum in GeV/c, t is the square of the momentum transfer in $({\rm GeV}/c)^2$, A is the forward elastic cross section, and $b(p)$ is the elastic-scattering slope parameter in $({\rm GeV}/c)^{-2}$. The slope parameter is represented by $b(p)=36.8-33.8p\ ({\rm GeV}/c)^{-2}$.

To obtain the target-length correction factor (ϵ_t), the path length traveled by the $\bar{n}$ in hydrogen was recorded for each event. The factor $\epsilon_t(p)$ is then given by the ratio of observed path lengths averaged over intervals in p divided by the maximum path length (50 cm). Numerical results are given in Table I. The slight momentum dependence arises from elastic scattering corrections to the path length.

The elastic-scattering correction ϵ_s^T needed to correct the CA (target full) yield was obtained from antineutrons which were initially headed for the calorimeter and scattered in the liquid hydrogen. The total number of such antineutrons is designated n_s. The correction for the total cross section (ϵ_s^T) depends on the number of scattered antineutrons which hit the calorimeter, since they must be subtracted from the target full yield. If n_c is the total number of antineutrons available to hit the calorimeter (i.e., those that do not annihilate in the hydrogen), then the correction can be expressed as

$$\epsilon_s^T=(n_c-n_s)/(n_c-n_m)\ . \tag{A1}$$

Numerical results are given in Table II.

[1]B. Gunderson, J. Learned, J. Mapp, and D. D. Reeder, Phys. Rev. D **23**, 587 (1981).
[2]T. Kalogeropoulos and G. S. Tzanakos, Phys. Rev. D **22**, 2585 (1980).
[3]T. Armstrong *et al.*, Phys. Lett. **175B**, 383 (1986).
[4]Y. Y. Xue, Ph.D. dissertation, University of Houston, 1985.
[5]A. T. Hicks, Ph.D. dissertation, The Pennsylvania State University, 1986.
[6]E. Fermi and C. N. Yang, Phys. Rev. **76**, 1739 (1949).
[7]R. A. Bryan and B. L. Scott, Phys. Rev. **135B**, 434 (1964).
[8]M. M. Nagels, T. A. Rijken, and J. J. de Swart, Phys. Rev. D **12**, 744 (1975).
[9]M. Lacombe *et al.*, Phys. Rev. D **12**, 1495 (1975).
[10]W. W. Buck, C. B. Dover, and J. M. Richard, Ann. Phys. (N.Y.) **121**, 47 (1979); C. B. Dover and J. M. Richard, *ibid.* **121**, 70 (1979); C. B. Dover and M. C. Zabek, *ibid.* **130**, 70 (1980).
[11]C. B. Dover, in *Intersections between Particle and Nuclear Physics—1986,* proceedings of the Second Conference, Lake Louise, Canada, 1986, edited by D. F. Geesaman (AIP Conf. Proc. No. 150) (AIP, New York, 1986), p. 272.
[12]C. B. Dover and J. M. Richard, Phys. Rev. D **17**, 1770 (1978).
[13]R. A. Bryan and R. J. N. Phillips, Nucl. Phys. **B5**, 201 (1968).
[14]C. B. Dover and J. M. Richard, Phys. Rev. C **21**, 1466 (1980).
[15]C. B. Dover (private communication).
[16]J. Côte *et al.*, Phys. Rev. Lett. **48**, 1319 (1982).
[17]A. M. Green and J. A. Niskanen, in *International Review of Nuclear Physics,* edited by T. T. S. Kuo (World Scientific, Singapore, 1984), Vol. 2; A. M. Green and J. A. Niskanen, in *Progress in Particle and Nuclear Physics,* edited by A. Faessler (Pergamon, New York, 1986).
[18]V. Chaloupka *et al.*, Phys. Lett. **61B**, 487 (1976).
[19]W. Brückner *et al.*, Phys. Lett. **67B**, 222 (1977).
[20]R. P. Hamilton *et al.*, Phys. Rev. Lett. **44**, 1182 (1980).
[21]C. Amsler *et al.*, in *Physics with Low Energy Cooled Antiprotons,* edited by U. Gastaldi and R. Klapisch (Plenum, New York, 1984), p. 375.
[22]E. Jastrzembski *et al.*, Phys. Rev. D **23**, 2784 (1981).
[23]D. I. Lowenstein *et al.*, Phys. Rev. D **23**, 2788 (1981).
[24]T. Brando *et al.*, Phys. Lett. **158B**, 505 (1985).
[25]F. Balestra *et al.*, Nucl. Phys. **A452**, 573 (1986).
[26]H. Raben, T. ter Elst, R. Timmermans, and J. J. de Swart (private communication).
[27]A. M. Green and J. A. Niskanen (private communication).
[28]A. Faessler (private communication).
[29]A. S. Clough *et al.*, Phys. Lett. **146B**, 299 (1984).
[30]R. P. Hamilton *et al.*, Phys. Rev. Lett. **44**, 1179 (1980).